ADVANCED FUNCTIONAL MATERIALS
www.afm-journal.de

Layer-by-Layer Fabrication of Nanowire Sensitized Solar Cells: Geometry-Independent Integration

Krishna P. Acharya, Zhiqiang Ji, Terry G. Holesinger, Jeffrey A. Crisp, Sergei A. Ivanov, Darrick J. Williams, Joanna L. Casson, Milan Sykora, and Jennifer A. Hollingsworth**

Thin film solar cells that are low in cost but still reasonably efficient comprise an important strategy for reaching price-performance ratios competitive with fossil fuel electrical generation. Sensitized solar cells – most commonly dye but also semiconductor nanocrystal sensitized – are a thin film device option benefitting from lost cost material components and processing. Nanocrystal sensitized solar cells are predicted to outpace their dye-based counterparts, but suffer from limited availability of approaches for integrating the nano-sensitizers within a mesoporous oxide anode, which effectively limits the choice of sensitizer to those that are synthesized in situ or those that are easily incorporated into the oxide framework. The latter methods favor small, symmetric nanocrystals, while highly asymmetric semiconductors (e.g., nanowires, tetrapods, carbon nanotubes) have to date found limited utility in sensitized solar-cell devices, despite their promise as efficient solar energy converters. Here, a new strategy for solar cell fabrication is demonstrated that is independent of sensitizer geometry. Nanocrystal-sensitized solar cells are fabricated from either CdSe semiconductor quantum dots or nanowires with facile control over nanocrystal loading. Without substantial optimization and using low processing temperatures, efficiencies approaching 2% are demonstrated. Furthermore, the significance of a 'geometry-independent' fabrication strategy is shown by revealing that nanowires afford important advantages compared to quantum dots as sensitizers. For equivalent nanocrystal masses and otherwise identical devices, nanowire devices yield higher power conversion efficiencies, resulting from both enhanced light harvesting efficiencies for all overlapping wavelengths and internal quantum efficiencies that are more than double those obtained for quantum dot devices.

1. Introduction

Semiconductor nanocrystal sensitized solar cells (NCSSCs) comprise an alternative to the more common dye-sensitized solar cells (DSSCs). The substitution of inorganic semiconductors for molecular dye compounds as the visible (to near-infrared) light sensitizer has the potential to afford better overall device efficiencies. NC absorption properties can be easily optimized to match the solar spectrum, including extension into the infrared, while their electronic structure can be easily matched to the band offsets of the electron and/or hole-conducting materials in the device, enhancing prospects for efficient charge injection and collection. The realized device efficiencies depend in large part on creating an intimate mixture of the nanoscale semiconductor particles and a mesoporous oxide film, which serves as the anode. Here, the light-absorbing nanocrystals must be electronically coupled with the electron-conducting oxide framework for efficient charge injection, as well as present in sufficient quantity to effectively absorb solar radiation.

NCSSC semiconductor-oxide mixtures have previously been prepared by two general approaches –in situ or ex situ incorporation of the semiconductor. The former

K. P. Acharya, J. A. Crisp, S. A. Ivanov, D. J. Williams, J. A. Hollingsworth
Materials Physics and Applications Division: Center for Integrated Nanotechnologies
Los Alamos National Laboratory
Los Alamos, New Mexico 87545, USA
E-mail: jenn@lanl.gov

T. G. Holesinger
Materials Physics and Applications Division: Materials Synthesis & Integrated Devices
Los Alamos National Laboratory
Los Alamos, New Mexico 87545, USA

J. L. Casson
Chemistry Division:
Physical Chemistry & Applied Spectroscopy
Los Alamos National Laboratory
Los Alamos, New Mexico 87545, USA

Z. Ji, M. Sykora
Chemistry Division:
Inorganic Isotope & Actinide Chemistry
Los Alamos National Laboratory
Los Alamos, New Mexico 87545, USA
E-mail: sykoram@lanl.gov

DOI: 10.1002/adfm.201401225

entails directly growing semiconductor nanocrystals within the oxide framework, either porous-TiO_2 or ZnO, using successive ionic layer adsorption and reaction or chemical bath deposition methods.[1–5] In contrast, the latter involves first synthesizing the semiconductor nanocrystals and then incorporating them into the porous oxide.[6–8] The in situ approach has generally afforded comparatively higher device efficiencies, with the ex situ approach often suffering from lower nanocrystal loading and/or poor electronic coupling between the nanocrystals and the oxide due to the presence of intervening molecular 'ligands,' which are present on the nanocrystal surfaces.[9,10] However, the ex situ strategy offers in principle one distinct advantage – almost unlimited flexibility in choice of semiconductor nanocrystal composition, size and morphology, where these characteristics can be used to finely tune semiconductor bandgap, exciton relaxation dynamics, electron-hole spatial separation, etc. In this way, the ability to address the nanocrystal loading and nanocrystal-oxide coupling issues currently limiting ex situ approaches remains an important challenge for optimizing NCSSC efficiencies.

Several strategies have been used for the ex situ incorporation of semiconductor nanocrystals into the porous photoanode. These can be loosely categorized as linker- or inverse-linker-mediated adsorption, direct adsorption, and electrophoretic deposition approaches. The linker strategy has typically entailed pre-treating the porous oxide with a bifunctional linker, such as mercaptopropanoic acid (MPA), that is thought to 'anchor' the nanocrystals to the oxide via a thiol bridge. In this case, the nanocrystals are incorporated into the mesostructure by soaking the electrode in a nanocrystal solution for 24–96 h.[11–13] Conversely, the nanocrystals themselves can be treated with such a linker molecule. For example, Zhang et al. have recently demonstrated very high loadings and the highest efficiency for a CdSe quantum dot (QD) NCSSC using this approach. In this case the QDs were loaded onto the oxide from water, instead of the more typical non-polar solvent, which likely allowed the observed unusually rapid nanocrystal incorporation (2 h).[14] Direct adsorption strategies entail a similar 'soaking' step, but do not make use of linker molecules.[15] Finally, electrophoretic deposition (EPD) can be used to promote the incorporation of nanocrystals into the porous oxide structure.[13] This approach offers the benefit of an enhanced driving force for nanocrystal penetration, also allowing rapid infiltration (2 h), as well as a new ability to incorporate anisotropic nanocrystals – nanorods in addition to QDs. In this way, EPD represents a clear advance in providing 'morphological flexibility,' where NC shape constitutes a potentially important materials parameter for optimizing solar-cell efficiencies.[16] However, even the EPD approach is limited in its ability to facilitate incorporation of anisotropic nanomaterials into the porous oxide structures, as indicated by lower Cd/Ti ratios in the case of CdSe nanorod devices compared to CdSe QD devices.[13] Significantly, it is not apparent that any of the above approaches, which rely on nanocrystal transport through a tortuous mesoporous host, would allow the incorporation of highly anisotropic or geometrically complex structures, such as nanowires, tetrapods, octapods, etc.

Herein, we demonstrate an alternative ex situ approach to NCSSC fabrication that does not entail nanocrystal incorporation into a pre-fabricated photoanode, but, instead, involves simultaneous formation of the anode-sensitizer composite. We do so with both QD and nanowire (NW) CdSe sensitizers, demonstrating the effectiveness of this 'geometry-independent' approach for even highly anisotropic nanocrystal sensitizers. We obtain device efficiencies comparable to those reported for traditionally ex situ fabricated CdSe NCSSCs. We achieve this level of performance despite the fact that our approach precludes the use of high photoanode sintering temperatures (450–550 °C) that are used in the case of other NCSSC fabrication methods. Furthermore, we consistently observe better performance for our NW devices compared to their QD counterparts, prepared under the same conditions. Importantly, we show that this finding is due to the better light-harvesting properties of NWs compared to QDs (NW absorption cross-sections are ~1 order-of-magnitude higher than QDs on a volume-normalized basis)[17] as well as better charge-collection in NW devices, which may be related to the tendency of NWs to exhibit very efficient light-induced charge separation.[18] As we show herein, these dual opportunities for performance enhancement coupled with a new approach for NCSSC fabrication point the way to a low-cost, low-processing-temperature photovoltaic technology that uniquely permits use of the most efficient nanomaterial irrespective of particle geometry.

2. Results And Discussion

Our device structure is similar to conventional CdSe NCSSCs in that it makes use of a sulphide/polysulfide electrolyte as the hole scavenger and a platinum coated fluorine tin oxide (FTO)/glass counter electrode (**Figure 1**a,b). In contrast with conventional NCSSC devices, however, the nanocrystal-mesooxide absorber-anode couple is prepared directly from a solution-phase nanocomposite as shown schematically in Figure 1c (details are provided in Experimental Section). Briefly, CdSe nanocrystals (QDs or NWs) in octane are mixed with a TiO_2 suspension in ethanol with accurately controlled NC-to-TiO_2 mass ratios (see below). This mixture is then deposited layer-by-layer by way of spin-coating onto the transparent electrode (FTO glass that is itself coated with a thin, ~100 nm sintered TiO_2 film). Each mixed NC-TiO_2 layer is prepared by first depositing the nanocomposite followed by a series of steps to remove bulky nanocrystal growth ligands [here, trioctylphosphine oxide (TOPO), trioctylphoshine (TOP), and oleic acid (OA)] and replace them with small bifunctional ligands that are capable of adhering to both the oxide and the semiconductor components [here, 3-mercaptopropionic acid (3-MPA)].

More specifically, under continuous spinning (~2500 rpm), the nanocomposite is spun-cast followed by addition of 3-MPA in methanol and then methanol and finally octane. This cycle constitutes a single layer addition, and the process is repeated numerous times to build up several micrometers thick films (Figure 1c). After layer-by-layer deposition of the CdSe/TiO_2 composite films, ZnS is deposited into the porous films using a chemical bath process that has been shown previously to afford enhanced device efficiencies.[19,20] The addition of ZnS at this stage in device fabrication is thought to improve NCSSC performance as a result of improved passivation of the nanocrystal surfaces, enhanced carrier extraction and reduced back electron

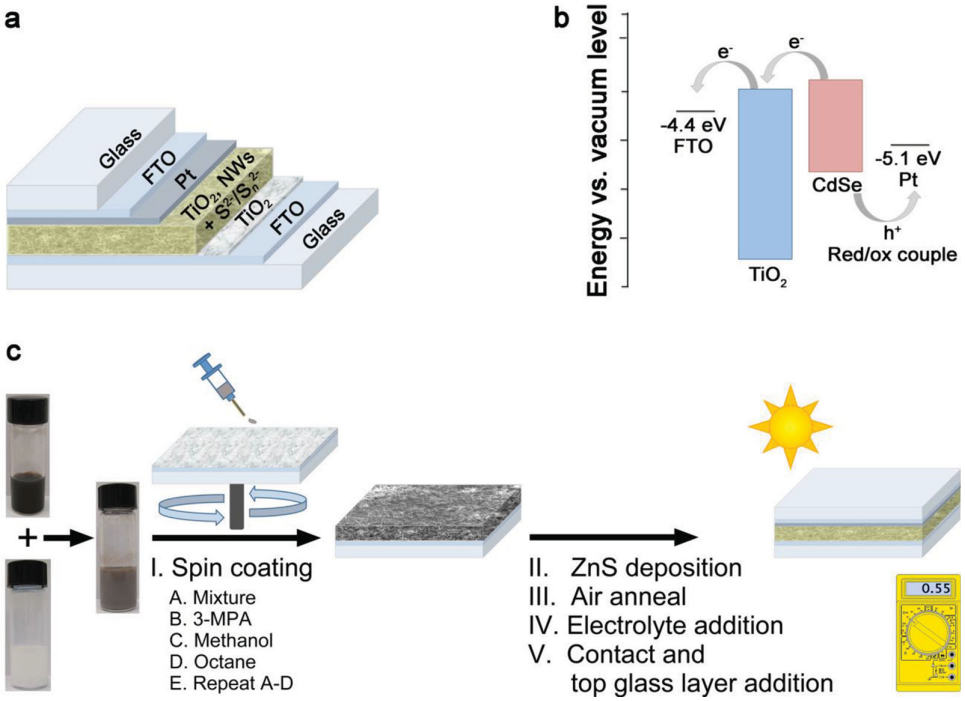

Figure 1. Geometry-independent NCSSC device fabrication. a) Schematic of the device structure (FTO: fluorine-doped tin oxide). b) Energy level diagram and flow of photogenerated charge carriers in fabricated NCSSCs. c) Layer-by-layer device fabrication from nanocrystal-TiO_2 composite slurries. Vials contain CdSe NWs (top), TiO_2 (bottom), and resulting mixture.

transfer.[21–23] The films are then heated to 300 °C for 10 minutes in air to partially sinter the TiO_2 mesostructure, remove remaining excess ligands and promote closer contact between the CdSe nanocrystals and the TiO_2 framework. The process by which this annealing temperature was selected is discussed below. The NCSSC is completed by the addition of the polysulfide electrolyte and the Pt counter electrode (Experimental Section).

The resulting composite film structures were characterized using scanning electron microscopy (SEM) and transmission electron microscopy (TEM) techniques to assess the overall film morphology, as well as the distribution of the CdSe component within the TiO_2 matrix. Despite the layer-by-layer approach to thin-film creation, no layering was observed in the resulting films (**Figure 2**a,b). Furthermore, film thickness varied minimally across the 0.36 cm^2 device area, e.g., 4.43 ± 0.12 μm and 4.40 ± 0.10 μm for 8-layer NW/TiO_2 and QD/TiO_2 films, respectively, as determined by step profilometry measurements. Cross-sectional TEM revealed comparable thicknesses to those obtained by the surface topography technique (Figure 2a-b), as well as providing insight into the NC-TiO_2 composite morphology. Specifically, at low-resolution, NWs are clearly seen to be distributed throughout the film structure, with a tendency to lie laterally within the otherwise non-directional matrix. At higher resolutions, both NWs and QDs were observed to form intimate mixtures with the TiO_2 framework (Figure 2c-f). We suggest that the NW-TiO_2 composite can be viewed as a "spoke-and-cluster" model where the NWs comprise spokes that span and link together otherwise unassociated TiO_2 clusters (Figure 2d inset). In contrast, the QD-TiO_2 composites are better thought of as simply "two-particle clusters" with the smaller QD particles (variably) coating the larger TiO_2 particles and clusters (Figure 2f inset).

Cross-sectional elemental line scans also show that the semiconductor nanocrystals are distributed essentially evenly throughout the film depth. That said, due to the tendency of CdSe NWs to span TiO_2 clusters, rather than conformally coat them as observed for CdSe QDs, we obtain "spikes" in the elemental depth profile versus the smoother profile obtained for QDs (**Figure 3**a,b). This observation can be further considered to result from the multi-dimensional nature of the NWs compared to QDs, i.e., NWs are both nanoscale (diameter) and micron-scale (length) in contrast with spherical QDs. Higher resolution elemental mapping of a region of a NW-TiO_2 composite reveals that the NWs do indeed both overlap and span regions occupied by TiO_2 (Figure 3c). Furthermore, Zn and S resulting from the ZnS coating applied after the composite-film is formed is present in both primarily TiO_2 and primarily CdSe regions (additionally evident in the lines scans), indicating that the chemical bath deposition process successfully coated all of the film constituents. Also, due to the nature of this approach, i.e., that composite films are prepared from simple mixtures of nanocrystals and TiO_2, nanocrystal loading can be easily tuned by simply changing the semiconductor:TiO_2 ratio in the starting solution-phase mixture. As discussed below, we investigated a range of loadings represented by Cd:Ti atomic ratios of ~0.03 to 0.44, spanning the range reported previously for linker-assisted incorporation and adsorption(e.g., 0.05 Cd:Ti,[12] electrophoretic deposition (~0.15 for QDs and ~0.09 for nanorods)[13] and ex situ ligand exchange (0.21 Cd:Ti)[14] methods.

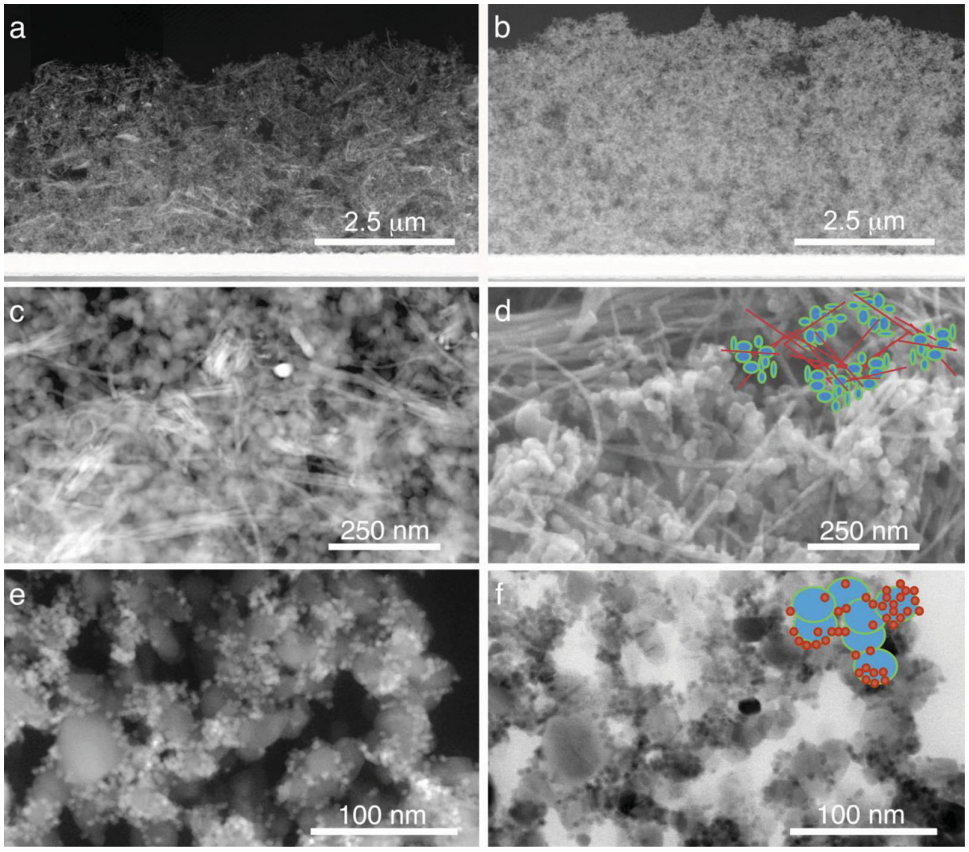

Figure 2. Electron microscopy images contrasting the structure of the NW and QD films. Low magnification Z-contrast scanning transmission electron microscopy (STEM) imaging shows the entire film cross-sections of the a) NW and b) QD based films. The fine structure of the NW films is shown with c) Z-contrast STEM and d) SEM images, with the generalized structure depicted by the inset in (d). e) Z-contrast and f) bright-field STEM images show the competing structure of the QD films, with the generalized structure depicted by the inset in (f).

Annealing temperature was an important criterion in ensuring optimal device performance. As mentioned above, conventional NCSSCs benefit from use of a high annealing temperature (450–550 °C), which affords a well-sintered TiO_2 matrix characterized by good electrical conductivity and optical clarity (minimal scattering). In that case, the semiconductor NCs are added after the oxide framework is sintered. In contrast, the presence of the semiconductor NCs initially in the TiO_2 may be expected to constrain annealing temperatures to those that do not damage the CdSe constituent. In **Figure 4**a we show current-voltage characteristics for a series of CdSe NW NCSSCs prepared identically except for the annealing temperature, which was varied from room-temperature (no annealing) to 400 °C. From room-temperature to 300 °C current density was observed to increase, with a decline only observed above 300 °C.

To understand the origin of the apparently deleterious impact of higher anneal temperatures on NCSSC device performance, we assessed CdSe NC crystal structure, oxidation processes, and ligand volatilization as a function of temperature by powder x-ray diffraction (XRD), thermogravimetric analysis (TGA), and differential scanning calorimetry (DSC). First, it was observed that whatever changes are taking place in the CdSe NCs (we focus here on NWs) with increasing temperature, these are not apparent in XRD patterns. The crystalline phase obtained by XRD remains unchanged in the range from room temperature to 400 °C (Supporting Information). In contrast, however, TGA reveals temperature-dependent mass changes as temperature is increased to 400 °C and above (Figure 4b), while DSC measurements show the energetics of the underlying processes. Specifically, there is a two-stage exothermic mass loss of 2.5% from ~240–370 °C followed by a broad exothermic mass gain (<1%) before complete decomposition ensues at temperatures above 600 °C. The initial mass loss is attributed to the desorption of MPA surface ligands (and/or remaining TOP, TOPO and OA ligands), while the ensuing small mass gain is due to partial oxidation of CdSe to form CdO and SeO_2.[24] At higher temperatures (Figure 4b: ~600–900 °C; 30.7% mass loss), oxidation is more complete and SeO_2 volatilizes (T_{sub} = 350 °C), leaving CdO as the final observed product as confirmed by XRD. Thus, as a result of annealing in air from room temperature to ~900 °C the following transitions are presumed to take place (Equation (1); L signifies ligand):

$$CdSe - L \xrightarrow{-L} CdSe \xrightarrow{+3O_2} 2CdO, 2SeO_2 \xrightarrow{-2SeO_2} 2CdO \quad (1)$$

The heating of the same material under N_2 (rather than air) results in a single-stage slightly endothermic mass loss at ~400 °C (see Supporting Information) due to the ligand removal without ligand or surface oxidation. No further mass

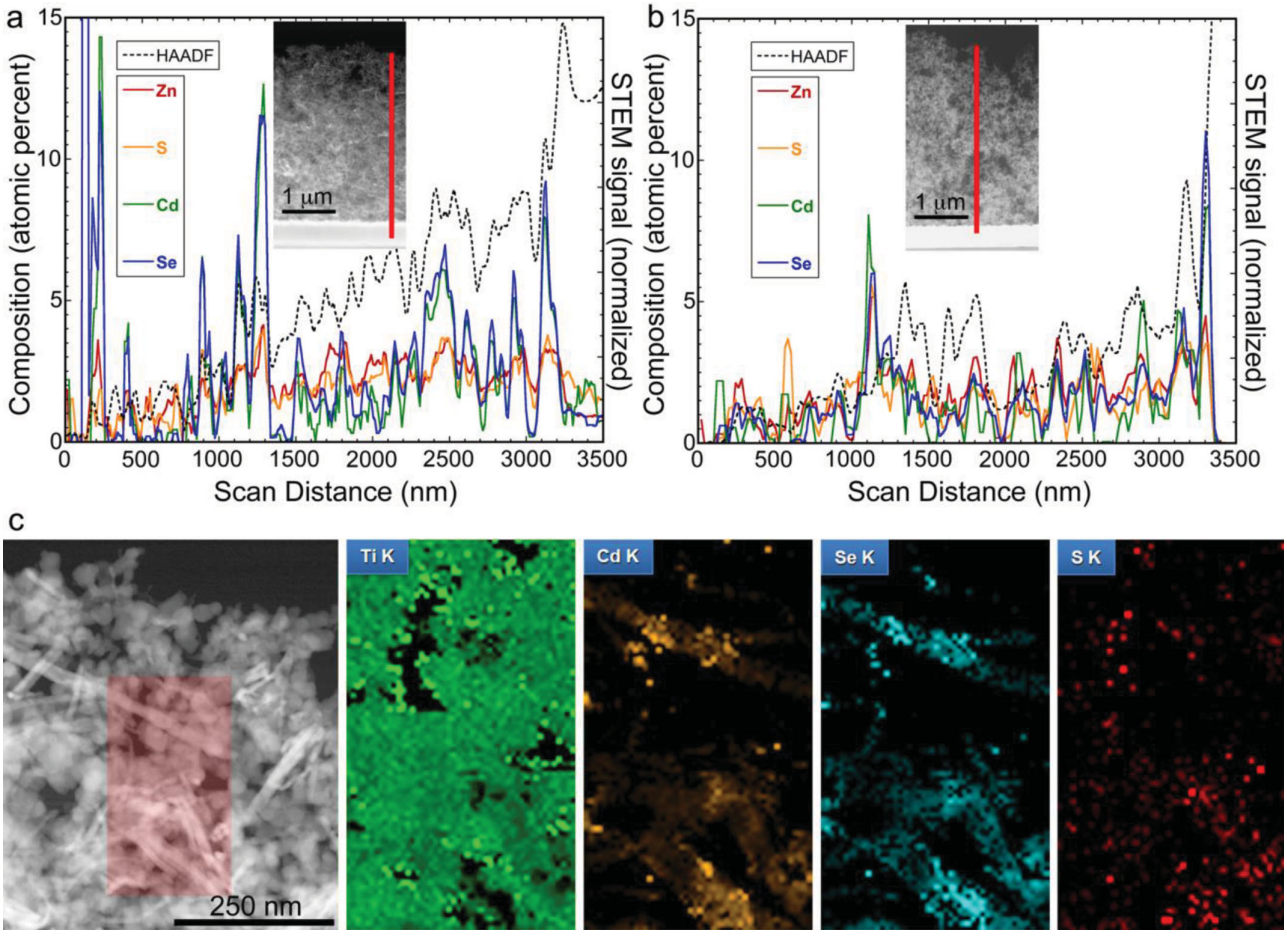

Figure 3. Measurements of local elemental composition by energy dispersive spectroscopy (EDS) in the STEM. Elemental line scans across a) NW and b) QD 8 layer films show the chemistry variations across the films, revealing relative locations of the embedded CdSe nanocrystals (as Cd and Se) and the ZnS overcoating (as Zn and S). Note: the HAADF detector signals increase with distance into the film (top to bottom) due to the natural increase in specimen thickness away from the open areas. c) EDS spectral images of the NW film (element identified is indicated in each inset) revealing overlap between the positions of CdSe nanocrystals, ZnS overcoating (as S) and the TiO_2 matrix (as Ti), where the region from which spectral images were obtained is shown by the Z-contrast STEM image (highlighted region).

loss was detected as temperature increases, which is consistent with the presented decomposition pathway.

Correlating temperature-dependent device characteristics with the processes of ligand loss and NC oxidation reveals that annealing temperatures below 400 °C afford enhanced performance as a result of enhanced CdSe-TiO_2 coupling deriving from ligand desorption, while films subjected to annealing temperatures higher than this suffer from partial (and ultimately complete) CdSe oxidation, which deleteriously impacts device performance.

As introduced above, the approach used here to prepare the nanocrystal-TiO_2 composite film allows us to tune the nanocrystal loading percentage by simply varying the amounts of CdSe and TiO_2 in the starting mixtures. By studying a range of NW loadings, we show that this parameter comprises another important factor affecting device performance. Specifically, we prepared composite films using CdSe NW to TiO_2 mass ratios corresponding to Cd:Ti atomic ratios ranging from 0.03 to 0.44. Relative device efficiencies obtained for this series are shown in **Figure 5**. Based on the results we conclude that an optimal Cd:Ti ratio is in the middle of the explored range, i.e., a Cd:Ti atomic ratio of 0.08, which corresponds to a maximum surface coverage of CdSe on TiO_2 of <20%.[14] Interestingly, the highest reported efficiencies for a CdSe QD NCSSC to date have been obtained for the highest yet reported Cd:Ti ratio and surface coverage, 0.21 and 34%, respectively.[14] The inability of higher Cd loadings to effect improved device performance in our case can likely be attributed to increased CdSe nanocrystal clustering at higher Cd:Ti ratios. As NWs self-associate they are in less direct contact with the TiO_2 mesostructure, which limits transfer of photogenerated carriers to the TiO_2 anode. Thus, we suggest that the method may be further improved by enhancing CdSe:TiO_2 associations within the nanocomposite mixture prior to film formation to reduce CdSe nanocrystal clustering and promote conformal surface coverage on the TiO_2.

Using the experimentally determined optimal annealing temperature and CdSe:TiO_2 ratio (obtained for CdSe NWs), we fabricated NCSSCs using either CdSe NWs or CdSe QDs. Photovoltaic performance results obtained under air mass 1.5 global (AM1.5 G) 1 sun illumination for each series are shown

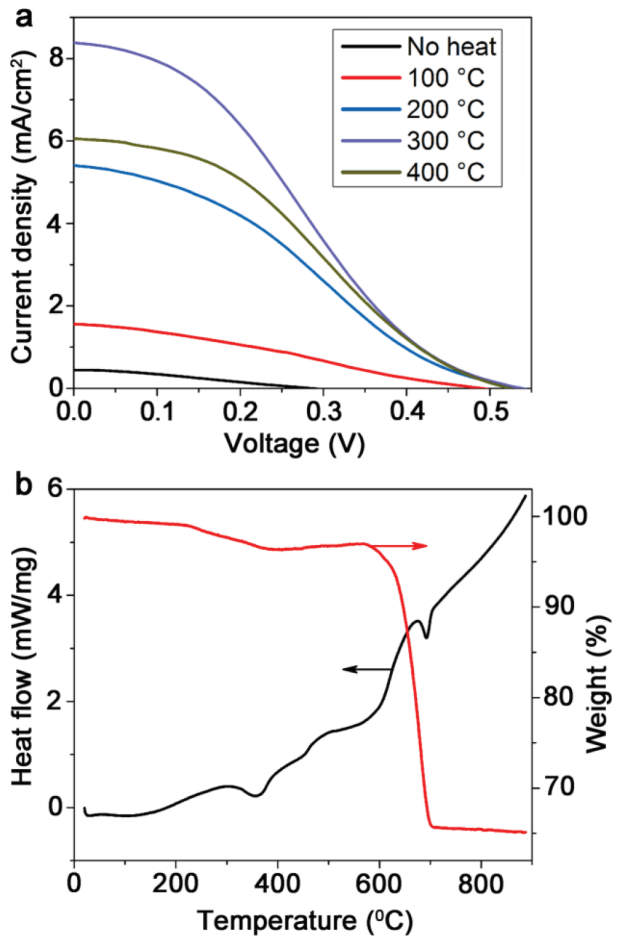

Figure 4. Impact of annealing temperature on device performance and material characteristics of the nanocrystal sensitizer. a) Current-voltage (*I-V*) characteristics of NW NCSSCs obtained for the range of annealing temperatures from room-temperature to 400 °C (as indicated in inset). The *I-V* characteristics were recorded while illuminating the solar cells with 100 mW/cm^2 simulated AM1.5 spectrum. b) TGA (red) and DSC (black) curves obtained for MPA-exchanged CdSe NWs in air.

in **Figure 6**a-d, with principal parameters listed in **Table 1** (open circuit voltage, V_{oc}; short circuit current density, J_{sc}; fill factor, *FF*; power conversion efficiency, *PCE*). As a function of composite-film thickness, current-voltage (I–V) characteristics reveal that V_{oc} remains relatively constant (NW NCSSC: 0.46–0.52 V; QD NCSSC: 0.43–0.54 V), while J_{sc} increases with number of deposition cycles up to a maximum reached at 16 cycles (NW NCSSC: 0.52 V, 10.39 mA/cm^2; QD NCSSC: 0.54 V, 7.47 mA/cm^2), and decreases for thicker films. Similarly, the 16-deposition-cycle films yield the highest external quantum efficiencies (*EQEs*), with maxima for both NW and QD devices occurring at ~480 nm (54% and 49%, respectively). These results suggest that the 16-layer device affords sufficient light absorption without compromising electron transport and collection; whereas, the thicker, 20-layer device suffers from losses in current density that likely occur as a result of increased carrier recombination with holes in the electrolyte and/or back-electron transfer to the semiconductor NW or QD absorber.

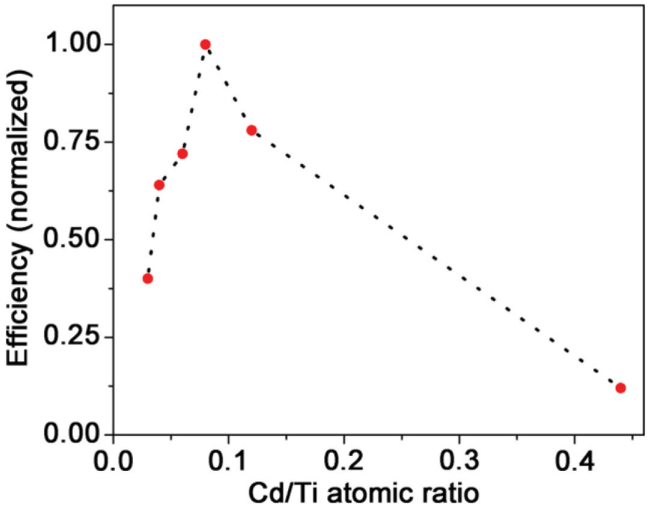

Figure 5. Impact of nanocrystal loading on device performance.

PCE also reaches a maximum for both NW and QD devices at 16 absorber layers: 1.60% and 1.10%, respectively (Table 1). These values compare favorably to efficiencies reported previously for similar NCSSC device constructs, where the combination of CdSe absorber, Pt counter electrode and polysulfide electrolyte has yielded PCEs from 0.4–1.7%.[11,13] It is worth noting that higher efficiencies can be achieved if, for example, the Pt counter electrode is replaced with a PbS (1.95–2.69%)[16] or Cu_2S (as high as 5.42%)[14] material. Significantly, multiple 16-layer NW and QD devices were fabricated and tested, and PCE was found to vary little: for six NW devices, PCE = 1.56 ± 0.10%, while for three QD devices, PCE = 1.13 ± 0.05%.

In all cases, for the same number of deposition cycles, the NW devices yielded higher values of J_{sc} and *EQE*. To better understand the origin of this trend we have determined the light harvesting efficiencies (*LHEs*) and internal quantum efficiencies (*IQEs*) of the QD and NW devices with varying number of deposition cycles. The *LHEs* were calculated from experimentally measured solar transmittances and reflectances of the films using Equation (2):

$$LHE(\lambda) = \left[(1 - \%T - \%R)\right] - \left[(1 - \%T(TiO_2) - \%R(TiO_2)\right] \quad (2)$$

In Equation (2), $\%T$ and $\%R$ are respectively the transmittance and the reflectance of the QD/TiO_2 or NW/TiO_2 films and the $\%T(TiO_2)$ and $\%R(TiO_2)$ are respectively the transmittance and reflectance of "blank" TiO_2 films prepared using the same number of deposition cycles. The *IQE* was calculated by dividing the measured *EQEs* by the corresponding *LHEs*. (Note: a separate set of *EQE* measurements from those shown in Figure 6 were used for this analysis.) The results are summarized in **Figure 7**a,b.

The results in Figure 7a show that the *LHEs* are consistently higher for the NW films compared to the QD films, regardless of the film thickness. This indicates that on equal weight basis the NWs are significantly better light absorbers than QDs. This is consistent with our comparison studies of absorptions of solutions prepared from equal weights of NWs and QDs (see Supporting Information) and with previous reports that showed

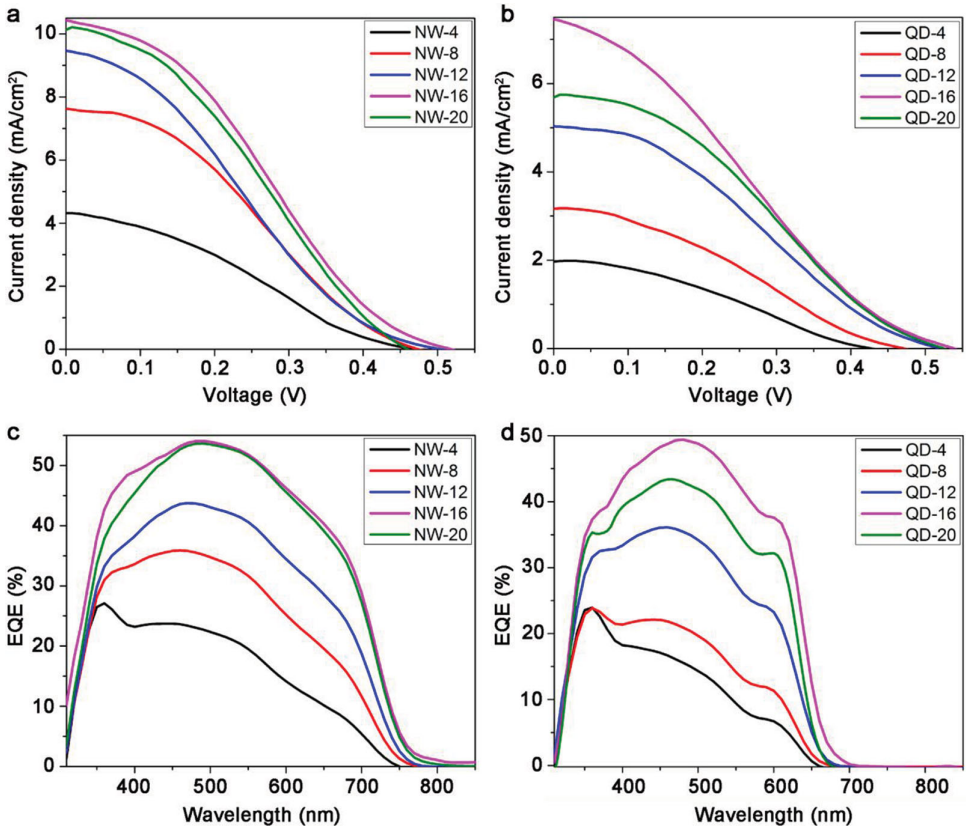

Figure 6. Photovoltaic performance as a function of deposition cycles for both NW and QD NCSSCs. a,b) I-V characteristics for devices comprising NW and QD sensitizers, respectively. Deposition cycle number is shown in inset. c,d) Measured external quantum efficiency (EQE) for NW and QD devices, respectively.

NW absorption cross-sections can be up to ~1 order-of-magnitude higher than QD absorption cross-sections on a volume-normalized basis.[17] We also point out that for both QDs and NWs the *LHE* gradually decreases in the spectral region below 500 nm with increasing film thickness. This effect is associated with the enhanced light scattering by the TiO_2 matrix in the thicker films (observable with naked eye), which prevents efficient harvesting of the incident light by both types of NCs (NWs and QDs) in this spectral region.

Table 1. Photovoltaic parameters of multilayer NCSSC devices prepared from either CdSe NWs or QDs.

Nanocrystal [number of layers]	Voc [V]	Jsc [mA/cm^2]	FF [%]	PCE [%]
NW (4)	0.47	4.39	29.65	0.61
NW (8)	0.47	7.66	31.84	1.15
NW (12)	0.50	9.42	26.08	1.24
NW (16)	0.52	10.39	29.76	1.60*
NW (20)	0.46	10.20	31.1	1.50
QD (4)	0.43	1.97	32.6	0.27
QD (8)	0.47	3.19	31.21	0.47
QD (12)	0.52	5.05	31.65	0.81
QD (16)	0.54	7.47	25.85	1.10
QD (20)	0.53	5.79	31.64	0.96

*By simply increasing anneal time from 10 min to 20 min, we obtained an efficiency of 1.83%.

In Figure 7b we show the *IQEs* for several NW and QD films. The *IQEs* only for thinner films are shown as for the thicker films the *IQE* curves were distorted due to significant light scattering. We observed that the *IQEs* are mostly independent of the film thickness and for all measured films the *IQEs* were consistently higher by a factor of 2–2.5 for NWs than for QDs. Since the *IQE* is a product of charge injection and charge collection efficiencies, our results indicate that charge injection and/or charge collection are about a factor of two more efficient in NW composites than in QD composites. We attribute this to a high exciton and/or charge mobility along the length of NWs,[18] which allows carriers to effectively diffuse to the optimal sites for NW-to-TiO_2 electron injection as well as hole collection by the electrolyte. This interpretation is also consistent with our observation of decreasing *EQEs* for thick films. While in QD devices the *EQE* shows dramatic drop when going from 16 to 20 layer films, most likely due to the inefficient hole collection in the parts of the film away from the film-electrolyte interface, this effect is less pronounced in NW films, where the holes can presumably more effectively diffuse to the electrolyte interface. More detailed understanding of the charge injection and collection processes in NW and QD films is an object of our future studies.

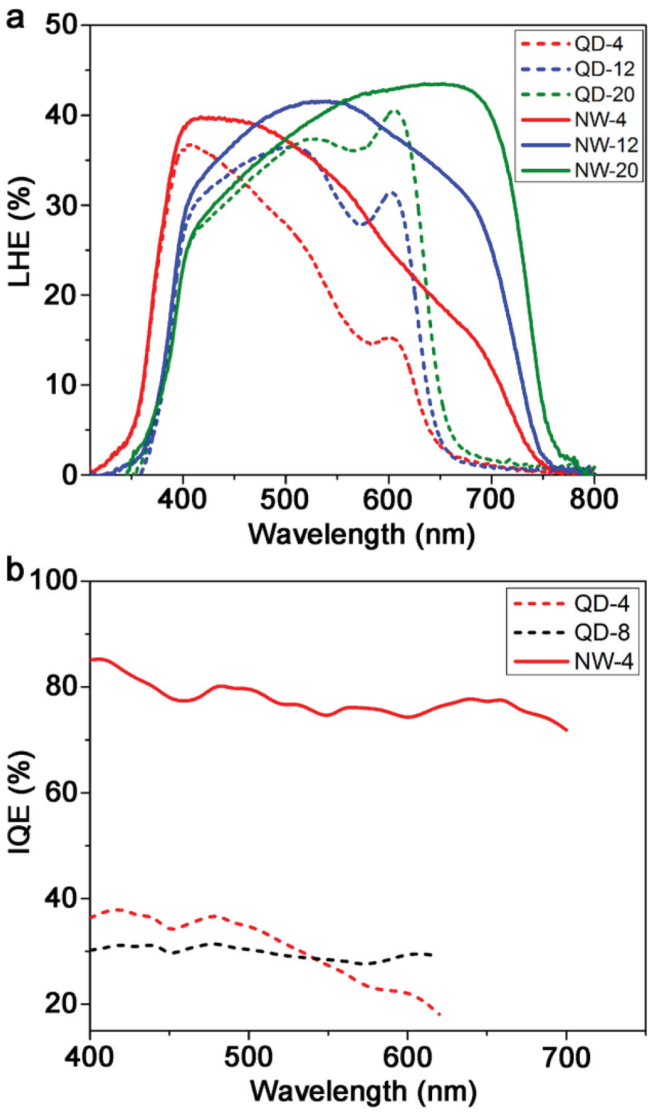

Figure 7. Assessing the origin of higher NW versus QD NCSSC device efficiencies by comparing both light harvesting and charge collection properties. a) Light harvesting efficiency (LHE) spectra for NW and QD sensitizers. For the same number of deposition cycles in all cases NWs absorb the incident light more efficiently than QDs. b) Internal quantum efficiency (IQE) obtained by dividing EQE by LHE. NW NCSSCs benefit from significantly enhanced charge collection compared to QD NCSSCs. (Insets show NW or QD and respective deposition layer number).

3. Conclusions

We have described a new, geometry-independent approach for incorporation of quantum-confined nanostructures into the sensitized solar cell architecture based on simultaneous formation of the anode-sensitizer composite. We showed that this approach can be effectively used to incorporate highly anisotropic NC sensitizers – such as NWs – into the sensitized solar cells, which is not possible using traditional sensitization approaches. We have further demonstrated that the solar cells based on NW composites yield substantially higher efficiencies compared to similar devices based on QDs, which we have attributed to both better light harvesting and charge collecting properties of the NW composites. Thus, the described approach opens a path for effective exploitation of nanostructures of various geometries in sensitized solar cells and for improvement of efficiencies of specific applications, such as, for example, previously described solar paints.[25]

4. Experimental Section

Materials: Bismuth (III) chloride ($BiCl_3$, 99.999% Acros), poly(1-hexadecene-co-1-vinylpyrrolidine) (PHD-co-PVP, ISP Technologies Inc., trade name: Ganex V216), cadmium oxide (CdO, 99.95% Alfa Aesar), 1,3-diisopropylbenzene (DIPB, 96% Acros), sodium bis(trimethylsilyl) amide ($Na[N(SiMe_3)_2]$, 1 M solution in tetrahydrofuran, Aldrich), tetrahydrofuran (THF, anhydrous, 99.9% Aldrich), selenium (Se, 99.999% Aldrich), oleic acid (OA, 90% Alfa Aesar), tri-n-octyl phosphine (TOP, 90% Fluka), tri-n-octyl phosphine oxide (TOPO, 99.0% Acros), toluene (99.9%, Fisher), ethyl alcohol (anhydrous, Fisher), isopropanol (anhydrous, 99.9% Acros), ethyl acetate (Fisher, 99.9%), diethyl ether (Aldrich, anhydrous 99.7%), 3-mercaptopropionaic acid (3-MPA, 99.0%, Fluka), zinc acetate ($Zn(CH_3COO)_2$, Aldrich 99.99%), sodium sulfide nonahydrate ($Na_2S{\cdot}9H_2O$, extra pure, Acros), potassium chloride (KCl, Fisher 99.5%), titanium (IV) tetraisopropoxide (TTIP, 98%, Acros), titanium dioxide (P25, Evonik Degussa), sulfur (S, 99.999%, Acros), chloroplatinic acid ($H_2PtCl_6{\cdot}6H_20$, Strem), n-octane (99%, Acros), triton X-100 (EMD). All chemicals were used as received without further purification. All reactions were performed under argon atmosphere using standard airfree Schlenk technique. Fluorine doped tin oxide glass (FTO, TEC 15, 12–14 Ω/sq) was obtained from Pilkington Glass.

Synthesis of Bi Nanocrystals: Bi nanocrystals (NCs) were synthesized using a procedure reported by Wang and Buhro.[26] A 25% by weight PHD-co-PVP solution was made by dissolving 3.75 g of the polymer in 13.1 mL DIPB. 5 g of this solution was degassed in a three-neck flask at 80 °C for one hour. The flask was switched to argon and heated to 200 °C. At this point a solution prepared by mixing 0.071 g $BiCl_3$ in 0.57 mL THF and 0.73 mL 1M $Na[N(SiMe_3)_2]$ in THF was injected. Before injection, a needle was inserted to expel THF from the reaction mixture. The reaction mixture was continuously heated at 200 °C for 6 hours. Resulting Bi NCs were cleaned three times by dissolving in toluene and precipitating with methanol. Finally, Bi NCs were dissolved in toluene and stored in a glovebox freezer. The diameter of Bi NCs as determined by TEM analysis was ~14.4 nm (Figure S1).

Synthesis of CdSe NWs and QDs: Colloidal CdSe nanowires (NWs) and CdSe quantum dots (QDs) were synthesized using modifications of known surfactant-mediated hot-injection methods. CdSe NWs were grown using the solution-liquid-solid (SLS) method, employing Bi NC catalysts.[27] Growth was optimized at different precursor ratios. It was observed that a lower Cd to Se (1:9) ratio favors the formation of short and branched NWs along with excess QDs. A higher Cd to Se ratio (9:1) produced longer straight wires; however, the limited amount of Se produced lesser yields. An equal molar ratio of Cd and Se produced good quality of CdSe NWs in an acceptable yield. Therefore, for all solar cell fabrication purposes, NWs were synthesized using one-to-one Cd to Se molar ratio. In a typical NW synthesis, 108 mg CdO (0.84 mmol), 9.0 g of TOPO, and 0.75 mL OA were degassed for 1 hour at 80 °C in a three neck flask. The flask was switched to argon and the temperature was increased to 280 °C and heated until CdO is converted to an optically clear cadmium oleate solution. At this point, a solution made by mixing 0.84 mL of 1 M TOP-Se (0.84 mmol), 0.6 mL TOP, and 0.3 mL Bi NCs with absorbance ~0.90 at 500 nm (measured with 1 mm path length) was injected. The flask was heated for 3 minutes and the heating mantle was removed. When the temperature was dropped to 90 °C, 9 mL toluene followed by 20 mL methanol were added and the resulting mixture centrifuged. The precipitate was dissolved in 15 mL toluene, and 20 mL methanol was added and the mixture again centrifuged. The solid product contains a mixture of CdSe NWs and QDs as evidenced by the presence of both a strong QD emission peak at ~600 nm and a weaker

NW peak at ~702 nm in the photoluminescence spectrum. QDs were subsequently essentially quantitatively removed by careful size-selective precipitation using isopropanol; the removal of ~all QDs was verified by the elimination of the QD peak from the photoluminescence spectrum. TEM analysis also confirmed the NW-pure product. The viscous and oily NW solution was further cleaned using a mixture of diethyl acetate and diethyl ether (4:1), and, finally, the NWs were dissolved in 12 mL octane. A freely flowing NW solution in octane was essential for making good quality NW film. CdSe QDs were synthesized using the NW procedure but eliminating the addition of Bi NCs. The NWs produced by the above procedure were ~8.5 nm in diameter, while the QDs produced in the absence of the Bi catalyst particles (but otherwise identical conditions to ensure equivalency in ligand content and Cd:Se ratio, barring those induced by the different modes of growth: flux mediated versus homogeneous nucleation and growth, respectively) were ~4.4 nm in diameter. TEM images, absorbance and emission spectra of NWs and QDs are shown in Figure S2.

Layer-by-layer Film Fabrication: FTO substrates (2.5 cm × 2.5 cm) were first wiped with ethanol and sonicated in a 2% triton solution in nanopure water and subsequently washed with nanopure water. Then, the substrates were sonicated successively in acetone and isopropanol for 15 minutes each. A TiO_2 suspension (46 mg/mL) was made by sonicating TiO_2 nanoparticles (0.880 g) in ethanol (19 mL) for 30 minutes. Titanium (IV) isopropoxide (0.13 mL) was added and the mixture sonicated for an additional 30 minutes. One drop TiO_2 suspension was spin coated onto the FTO substrate to create a hole-blocking layer. The FTO with the thin TiO_2 layer was heated at ~450° C for one hour to promote good conductivity. In a typical NW/TiO_2 composite film fabrication process, 1.6 mL (6.4 mg/mL) CdSe NW solution in octane is mixed with 1.2 mL (46 mg/mL) TiO_2 suspension, resulting in a composite mixture with a Cd/Ti ratio of 0.088 that is then sonicated for 30 minutes. Composite films are prepared layer-by-layer on the TiO_2 coated and sintered FTO/glass substrates. Each layer deposition entails spin-coating (at ~2500 rpm) in the following sequence: (i) 3 drops nanocomposite, (ii) 6 drops 2% 3-MPA in methanol, (iii) 10 drops methanol, and (iv) 10 drops octane. All materials were dropped while the substrate was spinning; one complete cycle of this sequence is termed as 'one layer.' The amount of material coated during, for example, 8 layer cycles for both NW and QD composite films was ~500 μg/cm^2. After addition of 8 layers, the substrate was split into four equal pieces and three of those pieces were used for further coating to generate 12, 16 and 20 layer films, respectively. 4-layer devices were prepared on separate substrates. QDs/TiO_2 nanocomposite films were prepared following the same procedure. Absorbance spectra for NW and QD solutions containing equivalent masses per unit volume are shown in Figure S3. Note: the addition of titanium (IV) isopropoxide to the TiO_2 slurry was found to enhance the optical quality of the resulting NW/TiO_2 films. QD/TiO_2 films did not require its addition, though for consistency TTIP was added in both cases.

ZnS Coating, Annealing and Device Assembly: The resulting multi-layer films were treated with two cycles of ZnS deposition using a chemical bath method. Films were dipped into a zinc acetate solution (0.1 M) for two minutes, washed with methanol, and then dipped in sodium sulfide solution (0.1 M) containing 1:1 water/methanol for two minutes, followed by a second methanol wash. The device area (0.36 cm^2) was made by scrapping off the film in the regions outside the designated area. The films were then annealed in air at 300 °C for 10 minutes. Platinum counter electrodes were prepared by spreading a few drops of 5 mM chloroplatinic acid in 2-propanol on FTO/glass followed by heating at ~400 °C for 1 h. Solar cells were assembled from the film, a Parafilm spacer (thickness 125 μm), and a polysulfide redox couple (S_2^-/S_n^{2-}). The polysulfide electrolyte was prepared by mixing Na_2S (2 M), S (2 M), and KCl (0.2 M) in water and methanol (7:3).[6] Photovoltaic parameters of eight-layer NWSSCs with different annealing temperatures, ZnS cycles, and annealing times are shown in Table S1, Table S2, and Table S3, respectively.

Characterization: Absorbance spectra were recorded using a CARY UV-Vis-NIR and NanoDrop 2000c spectrophotometers and emission spectra were recorded using NanoDrop 3300 fluorospectrometer. The morphology and composition of the films were examined using an FEI Inspect scanning electron microscope (SEM), a Tecnai TF30 (scanning) transmission electron microscope ((S)TEM), and a JEOL 2010 TEM. Cross-sectional (S)TEM specimens of whole films were prepared by cutting films into narrow strips and gluing together (M-Bond 610) face-to-face. This was then glued between two pieces of Si, allowed to cure, and then shaped to fit into a 3 mm diameter stainless steel tube. The tube was then sliced into discs that were then uniformly thinned down to approximately 120 μm. Then, each side was dimple-polished (South Bay D500i) leaving a remaining 15 μm in the middle. Final thinning to produce an electron transparent sample was by cryo ion milling (Gatan PIPs). Images of the NWs and QDs by themselves were obtained by using dilute solutions that were drop cast onto carbon coated copper grids from which TEM images of wires and dots were obtained. Fourier transform infrared spectra (FTIR) were measured using Nicolet 6700 spectrometer by placing solid sample on the surface of a diamond attenuated total reflectance FTIR cell. X-ray powder diffraction (XRD) measurements were obtained using a Rigaku Ultima III diffractometer that employs a Cu Kα (λ = 1.5406 Å) x-ray source. The powder sample was kept on a glass and the data were collected in the continuous scan mode in parallel beam slit geometry over the 2° from 10 to 90°. External quantum efficiency (EQE) spectra were measured with the monochromatic excitation from xenon arc lamp using a setup (QEX7) from PV Measurements, Inc. Current density-voltage (J-V) characteristics were measured under AM1.5 G (100 mW/cm^2) solar simulator using I-V data acquisition system from PV Measurements, Inc. Devices were masked except the active area during J-V measurements. The light intensity was calibrated using a National Renewable Energy Laboratory calibrated silicon photodiode. Differential Scanning Calorimetry (DSC) and Thermogravimetric Analysis (TGA) measurements were performed on a Netzsch simultaneous TGA/DSC analyzer, model STA 449 F1, using platinum/rhodium alloy crucibles. The heating rate for the sample was 10°/min under 150 mL/min of air flow (or N_2 for some samples) mixed with 50 mL/min of N_2, a protective flow of gas over the instrument's balances.

Supporting Information

Supporting Information is available from the Wiley Online Library and includes: TEM images and optical data of nanocrystal starting materials; additional SEM image views of composite structures; XRD patterns; FTIR spectra; data tables of device-fabrication-parameter-dependent photovoltaic parameters; TGA and DSC profiles.

Acknowledgments

K.P.A., Z.J., J.L.C., J.A.C., M.S and J.A.H. acknowledge partial support by the Los Alamos National Laboratory Directed Research and Development (LDRD) Program. T.G.H, S.A.I and D.J.W. were supported by the Center for Integrated Nanotechnologies (CINT), a US DOE Office of Science User Facility and Nanoscale Science Research Center (NSRC). This work was performed, in part, at CINT. We thank Antonya Sanders for assistance colorizing our 'wired-up' TiO_2 films.

Received: April 16, 2014
Revised: July 11, 2014
Published online: August 28, 2014

[1] Q. Zhang, X. Guo, X. Huang, S. Huang, D. Li, Y. Luo, Q. Shen, T. Toyoda, Q. Meng, *Phys. Chem. Chem. Phys.* **2011**, *13*, 4659.
[2] K. P. Acharya, H. Khatri, S. Marsillac, B. Ullrich, P. Anzenbacher, M. Zamkov, *Appl. Phys. Lett.* **2010**, *97*, 201108.

[3] T. Zewdu, J. N. Clifford, J. P. Hernandez, E. Palomares, *Energy Environ. Sci.* **2011**, *4*, 4633.
[4] J. W. Lee, D. Y. Son, T. K. Ahn, H. W. Shin, I. Y. Kim, S. J. Hwang, M. J. Ko, S. Sul, H. Han, N. G. Park, *Sci. Rep.* **2013**, *3*, 1050.
[5] Y.-L. Lee, T.-S. Lo, *Adv. Funct. Mater.* **2009**, *19*, 604.
[6] Z. Pan, H. Zhang, K. Cheng, Y. Hou, J. Hua, X. Zhong, *ACS Nano* **2012**, *6*, 3982.
[7] R. Robel, V. Subramanian, M. Kuno, P. V. Kamat, *J. Am. Chem. Soc.* **2006**, *128*, 2385.
[8] J. Chen, J. L. Song, X. W. Sun, W. Q. Deng, C. Y. Jiang, W. Lei, J. H. Huang, R. S. Liu, *Appl. Phys. Lett.* **2009**, *94*, 153115.
[9] H. Wang, C. Luan, X. Xu, S. V. Kershaw, A. L. Rogach, *J. Phys. Chem. C* **2012**, *116*, 484.
[10] N. Fuke, L. B. Hoch, A. Y Koposov, V. W. Manner, D. J. Werder, A. Fukui, N. Koide, H. Katayama, M. Sykora, *ACS Nano* **2010**, *4*, 6377.
[11] I. Mora-Sero, S. Gimenez, T. Moehl, F. Fabregat-Santiago, T. Lana-Villareal, R. Gomez, J. Bisquert, *Nanotechnology* **2008**, *19*, 424007.
[12] L. A. King, D. J. Riley, *J. Phys. Chem. C* **2012**, *116*, 3349.
[13] A. Salant, M. Shalom, I. Hod, A. Faust, A. Zaban, U. Banin, *ACS Nano* **2010**, *4*, 5962.
[14] H. Zhang, K. Cheng, Y. M. Hou, Z. Fang, Z. X. Pan, W. J. Wu, J. L. Hua, X. H. Zhong, *Chem. Commun.* **2012**, *48*, 11235.
[15] S. Gimenez, I. Mora-Sero, L. Macor, N. Guijarro, T. Lana-Villarreal, R. Gomez, L. J. Diguna, Q. Shen, T. Toyoda, J. Bisquert, *Nanotechnology*, **2009**, *20*, 295204.
[16] A. Salant, M. Shalom, Z. Tachan, S. Buhbut, A. Zaban, U. Banin, *Nano Lett.* **2012**, *12*, 2095.
[17] V. Protasenko, D. Bacinello, M. Kuno, *J. Phys. Chem. B* **2006**, *110*, 25322.
[18] S. Schafer, Z. Wang, R. Zierold, T. Kipp, A. Mews, *Nano Lett.* **2011**, *11*, 2672.
[19] Q. Shen, J. Kobayashi, L. J. Diguna, T. Toyoda, *J. Appl. Phys.* **2008**, *103*, 084304.
[20] T. Zewdu, J. N. Clifford, E. Palomares, *Chem. Chem. Phys.* **2012**, *14*, 13076.
[21] G. Guijarro, J. M. Campina, Q. Shen, T. Toyoda, T. Lana-Villarreal, R. Gomez, *Phys. Chem. Chem. Phys.* **2011**, *13*, 12024.
[22] H. Zhu, T. Lian, *Energy Environ. Sci.* **2012**, *5*, 9406.
[23] I. Mora-Seró, S. Giménez, F. Fabregat-Santiago, R. Gómez, Q. Shen, T. Toyoda, J. Bisquert, *Acc. Chem. Res.* **2009**, *42*, 1848.
[24] D. A. Hines, M. A. Becker, P. V. Kamat, *J. Phys. Chem. C* **2012**, *116*, 13452.
[25] G. P. Matthew, I. V. Lightcap, P. V. Kamat, *ACS Nano* **2012**, *6*, 865.
[26] F. Wang, W. E. Buhro, *Small* **2010**, *6*, 573.
[27] Z. Li, O. Kurtulus, N. Fu, Z. Wang, A. Kornowski, U. Pietsch, A. Mews, *Adv. Funct. Mater.* **2009**, *19*, 3650.